

See Less, Drive Better: Generalizable End-to-End Autonomous Driving via Foundation Models Stochastic Patch Selection

Amir Mallak¹ Erfan Aasi² Shiva Sreeram² Tsun-Hsuan Wang² Daniela Rus² Alaa Maalouf^{1,2}

¹University of Haifa ²CSAIL, MIT

Correspondence: mallak002@gmail.com

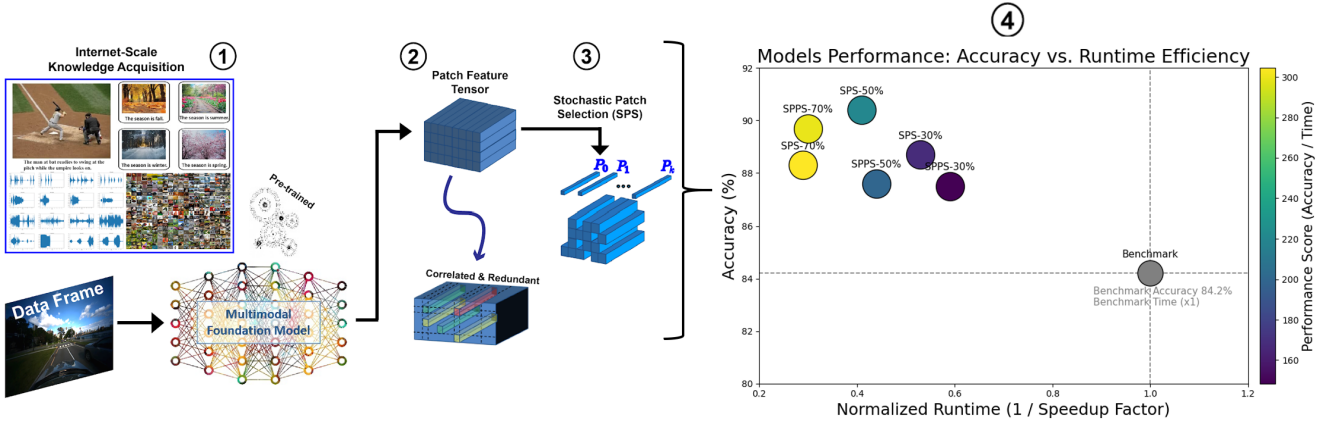


Figure 1. **Stochastic Patch Selection (SPS) in a nutshell.** (1) We use large vision-language models to extract patch-level features for input images. (2) These descriptors are often highly redundant and correlated. (3) SPS randomly masks a subset of descriptors, forcing the policy to learn based on different subsets and less correlation, improving efficiency ($2.4\times$ speedup), generalization (+6.2% performance), and enabling plug-and-play integration with downstream policies. In (4), we compare speed vs performance on different variants of SPS against SOTA.

Abstract

Recent advances in end-to-end autonomous driving show that policies trained on patch-aligned features extracted from foundation models generalize better to Out-Of-Distribution (OOD). We hypothesize that due to the self-attention mechanism, each patch feature implicitly embeds/contains information from all other patches, represented in a different way and intensity, making these descriptors highly redundant. We quantify redundancy in such (BLIP2) features via PCA and cross-patch similarity: 90% of variance is captured by 17/64 principal components, and strong inter-token correlations are pervasive. Training on such overlapping information leads the policy to overfit spurious correlations, hurting OOD robustness. We present Stochastic-Patch-Selection (SPS), a simple yet effective approach for learning policies that are more robust, generalizable, and efficient. For every frame, SPS randomly masks a fraction of patch descriptors, not feeding them to the policy model, while preserving the spatial layout of the remaining patches. Thus, the policy is provided with different stochastic but complete views of the

(same) scene: every random subset of patches acts like a different, yet still sensible, coherent projection of the world. The policy thus bases its decisions on features that are invariant to which specific tokens survive. Extensive experiments confirm that across all OOD scenarios, our method outperforms the state of the art (SOTA), achieving a 6.2% average improvement and up to 20.4% in closed-loop simulations, while being $2.4\times$ faster. We conduct ablations over masking rates and patch-feature reorganization, training and evaluating 9 systems, with 8 of them surpassing prior SOTA. Finally, we show that the same learned policy transfers to a physical, real-world car without any tuning.

1. Introduction and background

As autonomous-driving technology matures, end-to-end approaches emerged as a leading strategy [1, 2] embodying a transformative design philosophy: a single model handles everything, from perception to control. This approach (i) dispenses with many of the rigid assumptions imposed on individual submodules, and (ii) evaluates and optimizes performance against a single overarching objective, yielding a

more coherent and effective system.

From foundation models to driving polices. Recently, Wang et al. [3] showed that extracting patch-aligned (multimodal) features from a foundation model (FM) [4–6], for each input frame, and training a lightweight policy on those features, markedly improves out-of-distribution (OOD) generalization. To obtain patch features, they applied *masked* attention at a chosen layer (specifically, at the input to BLIP2’s Q-Former), so the mask guides the attention to focus on a single image patch. Repeating this operation for every patch yields a descriptor per patch. Since the descriptors come from the output layer that interfaces with the text encoder, they live in a shared vision–language space, enabling text-driven augmentation and robust policy debugging.

Patch-wise features are redundant. We posit that patch descriptors extracted from ViT backbones are intrinsically redundant and correlated. Before introducing the masked-attention layer, every patch embedding produced by the sub-ViT backbone has already attended to all other patches, as self-attention mixes information across tokens; each “patch feature” is no longer a purely local descriptor, as it carries a weighted summary of the entire scene, although the information is focused on this patch. This redundancy is detrimental when we hand the descriptors to the policy head: (1) Correlated inputs inflate the effective dimensionality of the feature space, making it harder for the policy network to disentangle the truly discriminative signals. (2) Overlapping information encourages over-fitting; the policy may memorize spurious correlations present in the duplicated context instead of learning robust, spatially grounded cues. Finally, (3) unnecessary redundancy wastes computation and memory, both during training and at inference time.

1.1. Our contributions.

We first empirically show that patch-features are redundant in Section 4.1 via similarity overlays, patch-wise correlations, and PCA explained-variance curves. Building on these insights, we propose **Stochastic-Patch-Selection (SPS)**, a lightweight, plug-and-play patch-masking strategy that improves both the efficiency and OOD generalization of policy learning; See Figure 1. Our main contributions are as follows.

- (i) **SPS:** At each frame, SPS randomly drops a fixed proportion of patch descriptors, forwards the untouched descriptors to the policy network, and crucially leaves their grid positions unchanged. Each unmasked subset forms a coherent yet distinct stochastic view of the scene, encouraging the policy to focus on stable/invariant, causally relevant cues instead of spurious correlations.

- (ii) **Robustness and efficiency gains over SOTA.** Across all OOD scenarios, SPS improves closed-loop driving success by an average of 6.2 %, and up to 20.4 %, while being 2.4×.
- (iii) **Comprehensive ablations at scale.** We train and evaluate 9 autonomous-driving systems under varied masking ratios and patch-reorganization schemes, identifying the design choices that maximize robustness; all variants except one surpassed the previous SOTA.
- (iv) **Sim-to-Real generalization.** We deployed SPS on a full-scale autonomous vehicle, showing a seamless transfer from simulation to a real car without tuning.

Notably, as SPS operates in a shared vision-language space, it inherits from [3] the support for text-conditioned perturbations/augmentation in the patches embedding space, yielding an additional 1.7 % performance boost.

2. Related work

End-to-end autonomous driving. Early work established that neural networks can map raw sensory inputs directly to low-level control [1, 2], with subsequent efforts exploring probabilistic objectives and uncertainty-aware control [7], stability/attention regularization [8], and safety-aware formulations using control barrier functions [9, 10]. While promising, end-to-end approaches typically demand large, diverse real-world datasets that are costly and risky to collect at scale [11, 12]. To mitigate this, photorealistic simulators like CARLA, AirSim, and Drake [13–15], and trace-driven interactive simulation such as VISTA [12], have become standard for training and evaluation. A complementary line replaces raw pixels with intermediate visual abstractions (affordances, semantics, lane topology) to simplify control [16–18]. In this space, “Drive Anywhere” [3] introduced a *foundation-model*-based pipeline that extracts rich, multimodal patch-aligned descriptors and feeds them to a lightweight policy head, showing strong OOD generalization. Our work builds on this FM-based formulation and aims to patch features *reduce redundancy* at train/inference time to improve OOD robustness without modifying or fine-tuning the FM.

Foundation models in robotics and vision. Large pre-trained vision language models are increasingly used as general-purpose perception and reasoning backbones, from language-conditioned manipulation and planning [19–23], video summarizations [24], and 3D/open-world scene understanding [25–27] to navigation and instruction following [28] and follow-and-detect pipelines [29–33]. Their cross-modal capacity also enables generative interfaces that tie vision and language [34–37]. Within autonomous driving, some prior work cautions that the temporal reasoning robustness of off-the-shelf VLMs is limited in settings that require strong temporal understanding [38]; therefore, de-

ploying them for driving tasks out of the box is not straightforward. This motivates learning downstream driving policies on top of features extracted from pretrained VLMs, rather than relying on end-to-end VLM reasoning. works increasingly leverage language-grounded or explainable representations/features/descriptors for introspection, learning, and counterfactual analysis [3, 28, 39–43]. We follow this trend in spirit, but use only frozen FMs (BLIP/BLIP-2 [4, 5], DINO [44, 45]) and intervene solely at the patch-descriptor interface to a small policy head—isolating our stochastic selection from FM training dynamics.

Positioning and novelty. Prior end-to-end policies [1, 2, 7–10] and FM-based driving frameworks [3, 28] have not treated *feature redundancy* in FM patch descriptors as a first-class lever for OOD robustness. Such patch embeddings from pretrained models can be obtained by: (i) *region-first* pipelines that segment the image (e.g., SAM/Mask2Former) and then pool features within each mask by an FM encoder (e.g., CLIP) [46–51]. These methods inherit sensitivity to segmentation quality and add extra compute stages. (ii) *patch-aligned* extraction directly from the backbone without external masks or fine-tuning [3, 28, 52], preserving spatial layout at token resolution and avoiding segmentation dependencies. Our contribution is orthogonal and complementary: we show that even strong patch-aligned descriptors, *are highly redundant*. We therefore introduce *Stochastic Patch Selection (SPS)*, a simple mechanism to handle such correlations, via a *post-FM* token-selection step that preserves spatial layout, reduces token count, and improves closed-loop OOD performance while reducing latency. SPS is architecture-agnostic, requires no FM fine-tuning. Evidence from PCA and inter-token-correlation analyses, ablations over masking/reorganization variants, and real-world transfer leads to a simple takeaway: for FM-derived patch features in driving, *less can be more*: carefully injected stochastic sparsity improves generalization without any overhead.

3. Method

We first provide the preliminaries.

3.1. Preliminaries

End-to-end driving as feature-based control. We model an autonomous-driving policy as a control function ϕ that maps a perception stream $F \in \mathbb{R}^{H \times W \times 3}$ of RGB frames to steering and throttle commands $u = \phi(F)$. Rather than operating on raw pixels, we feed ϕ a tensor of patch-aligned representations $F' = \text{Desc}(F) \in \mathbb{R}^{H' \times W' \times D}$ produced by a multimodal foundation model Desc , where (H', W') is the patch grid and D is the channel dimension, i.e., $u = \phi(F')$.

We now recall the masked-attention mechanism of [3], which enforces spatially selective mixing.

Multimodal patch-wise feature extraction [3]. Let Desc be a vision transformer of L layers and $N = H'W'$ be the number of non-overlapping patches. During a forward pass of Desc on F , the ℓ -th self-attention layer yields the query, key, and value matrices denoted by $Q_{\text{Desc}(F)}^\ell, K_{\text{Desc}(F)}^\ell \in \mathbb{R}^{N \times D_k}$ and $V_{\text{Desc}(F)}^\ell \in \mathbb{R}^{N \times D}$, respectively. To compute the feature of patch $j \in [N]$, Wang et al. [3] introduced (1) an attention mask $M^{(j)} \in [0, 1]^N$, where $M_i^{(j)} = 1$ preserves information from patch i and $M_i^{(j)} = 0$ excludes it, and (2) a parameter $r < 0$ controlling the suppression strength: the larger $|r|$, the stronger the masking effect. Forming the similarity matrix $G_{\text{Desc}(F)}^\ell = Q_{\text{Desc}(F)}^\ell K_{\text{Desc}(F)}^{\ell \top}$, the attention focus on the information defined by $M^{(j)}$ is:

$$G_{\text{Desc}(F)}^\ell \tilde{=} G_{\text{Desc}(F)}^\ell + (1 - M^{(j)})r, \quad (1)$$

where $M^{(j)} = [m^{(j)}, \dots, m^{(j)}]^\top$. This operation drives attention scores in $G_{\text{Desc}(F)}^\ell$ for patches with $m_i \approx 0$ down to r , thus masking them in the following softmax. The term $(1 - M^{(j)})$ adds 0 when the mask is 1 and r when it is near 0. The masked attention weights $\text{SoftMax}(\tilde{G})$ yield the desired descriptor through the remaining layers:

$$F'^{(j)} = \text{Desc}^{\ell \rightarrow}(\text{SoftMax}(\tilde{G}) V_{\text{Desc}(F)}^\ell). \quad (2)$$

Repeating this procedure for all j reconstructs $F' \in \mathbb{R}^{H' \times W' \times D}$.

Mask design. For a patch j , we set weight $M_i^{(j)} = f(d_{ij})$ where d_{ij} is the distance in the patch grid $\|(x_i, y_i) - (x_j, y_j)\|_2$, and f as a hard cutoff $1[d_{ij} \leq \alpha]$, or soft decays $2^{-d_{ij}}$ and $1/d_{ij}$, giving flexible locality.

3.2. Redundancy as low-rank structure

Let $F_c \in \mathbb{R}^{N \times D}$ denote the matrix of patch descriptors obtained by applying Desc to F , where $N = H'W'$ is the number of patches and D is the dimension of each descriptor (F_c is the reshaped F' to matrix form). Let \tilde{F}_c be the mean-subtracted matrix, and $\lambda_1 \geq \dots \geq \lambda_r > 0$ be the eigenvalues of the sample covariance $\Sigma = \frac{1}{N} \tilde{F}_c^\top \tilde{F}_c$, with rank $r \leq d$. The cumulative explained variance after the first $m \leq r$ components is

$$E(m) := \frac{\sum_{i=1}^m \lambda_i}{\sum_{i=1}^r \lambda_i}. \quad (3)$$

A rapidly saturating $E(m)$ for $m \ll d$ indicates a low-rank structure, hence redundancy among the patch descriptors. In Section 4.1 we empirically show that BLIP2 features reach 90% explained variance with 17 of 64 components ($E(17) > 0.9$). Even more, when using half of the patches with the highest ℓ_2 norm, the first 14 principal components explain 90% of the variance ($E(14) > 0.9$). A proof sketch and implementation details appear in Appx. A.1.

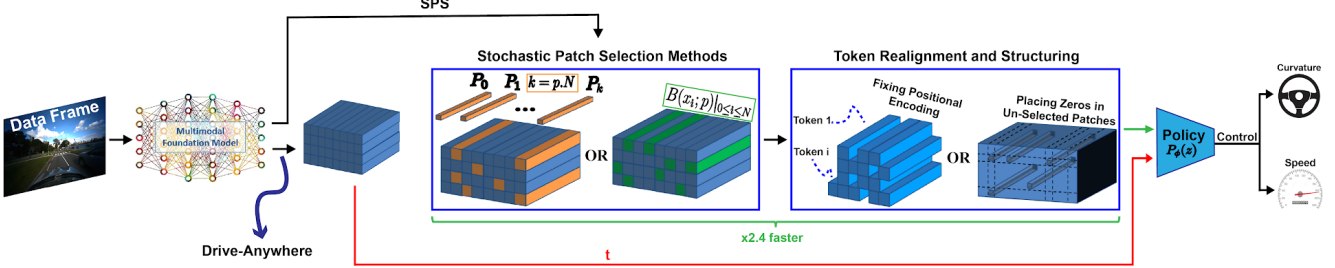


Figure 2. SPS algorithm vs Drive-Anywhere illustration. From left to Right. 1st: Input images are processed through a frozen foundation model to produce patch-level descriptors. 2nd: In Drive-Anywhere, the full tensor is forwarded unchanged to the policy. 3rd: In our approach, we introduce two patch selection strategies (uniform stochastic and matrix-based probability selection), followed by (4th) a restructuring phase: either masking unselected descriptors or removing them and adjusting positional encodings. Both versions preserve spatial semantics while significantly reducing runtime. SPS improves efficiency by a factor of $2.4\times$ while also boosting generalization.

3.3. Stochastic patch selection (SPS)

Reducing descriptor redundancy. As we saw, information about a scene is implicitly replicated across all tokens. The resulting redundancy (i) inflates the computation needed to extract *every* patch feature, (ii) encourages the policy to rely on spurious, correlated cues that collapse under distribution shift, and (iii) forces the policy to require every tiny detail of the full scene to provide a robust decision.

Our goal is therefore to *expose the policy*, at every input frame, to a fraction of the patch descriptors and withhold the others, via a token-level stochastic selection mechanism operating in the latent space of the foundation model, while maintaining the spatial layout of the remaining patches. Each random subset forms a different, yet still coherent, projection of the same scene, giving the policy a stream of stochastic but complete views. Consequently, the controller is trained to base its decisions on features that remain invariant to which specific tokens survive, yielding improved OOD robustness and lower compute, all while preserving spatial coherence and encouraging the use of robust, generalizable signals over exact token identity.

Let $N = H'W'$ denote the number of patch positions produced by the backbone Desc (see Sec. 3.1). Fix a *sampling rate* $\text{RATE} \in (0, 1]$. For every input frame t we:

1. **Sample a subset.** Uniformly at random, select exactly $k = \lceil \text{RATE} \cdot N \rceil$ patch indices, denoted $\Omega_t \subseteq \{1, \dots, N\}$ with $|\Omega_t| = k$.
2. **Compute descriptors.** Run the masked-attention extractor (Sec. 3.1) *only* for patches $i \in \Omega_t$, obtaining for every i , the descriptor $F'_i \in \mathbb{R}^D$.
3. **Build the sparse tensor.** Assemble $\tilde{F}' \in \mathbb{R}^{H' \times W' \times D}$:

$$\tilde{F}'_i = \begin{cases} F'_i, & i \in \Omega_t, \\ 0, & \text{otherwise,} \end{cases} \quad (4)$$

thereby *preserving the original spatial layout* so the policy head receives a tensor of fixed size.

Computational footprint. The expected fraction of evaluated descriptors is RATE, so feature extraction time scales linearly with the keep-rate. For example, $\text{RATE} = 0.4$ cuts the forward pass of the foundation model ViT_L backbone by $\sim 2.5\times$ without altering the policy architecture. The variant which fix the positional embedding at the VIT, also improve the runtime of the policy.

Overall. SPS turns a dense, patch-aligned representation into a *stochastically sparse*, yet spatially coherent, token sequence. By training the control policy on these variable but complete projections of the scene, we (1) reduce compute, (2) discourage reliance on redundant correlations, and (3) drive consistent gains in OOD generalization; see Section 4.3.

3.4. Ablations and variants

To understand the design space, we evaluate two additional variants of the above procedure.

(v1) Threshold masking. Instead of sampling exactly k indices, draw an i.i.d. vector $R \sim \mathcal{U}(0, 1)^{H'W'}$ and define

$$\Omega_t = \{i \mid R_i \leq \text{RATE}\}. \quad (5)$$

Each patch is sampled independently with probability RATE, so the expected keep-rate is RATE but the actual count fluctuates. This adds stochastic diversity at negligible cost.

(v2) Position-adjusted sparse sequence. After choosing Ω_t (either by fixed-count or threshold masking), *omit* the dropped tokens entirely and feed the policy only the descriptors that were actually computed. Each retained descriptor F'_i is augmented with its original positional embedding $p_i \in \mathbb{R}^D$ drawn from the ViT's full positional-embedding table, so the controller still knows *where* each token came from. This yields a variable-length input sequence that is shorter by a factor of RATE without inserting any zero vectors.

Figure 2 illustrates our method alongside its variants.

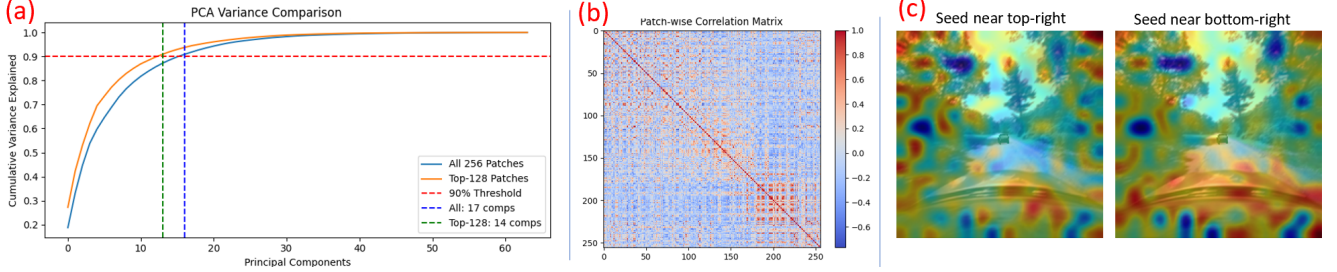


Figure 3. (a) Cumulative explained variance over principal components for all patches versus the top-128 patches selected by ℓ_2 norm. The red line marks 90%. Vertical markers indicate 17 and 14 components for all and top-128, respectively. (b) Patch-wise Pearson correlation matrix for one scenario. Strong off-diagonal correlation indicates widespread cross-patch redundancy. (c) Cosine-similarity overlays projected onto the image plane. Bright regions indicate patches whose descriptors are highly similar to the seed, visualizing global entanglement from self-attention.

3.5. SPS preserves scene semantics

Subspace preservation under uniform row sampling. If the variance of F_c concentrates in a few components, the patch descriptors (rows of F_c) lie near a low-dimensional subspace. If the row coherence is low, uniformly sampling enough rows preserves this principal subspace with high probability, hence the policy still receives descriptors that span the same semantics. We now show it formally.

Lemma 1 (SPS preserves the row-space under low rank and bounded coherence). *Let $F_c \in \mathbb{R}^{N \times d}$ be a centered data matrix with $\text{rank}(F_c) = r$, and let its (thin) singular value decomposition be $F_c = U_r \Sigma_r V_r^\top$, where $U_r \in \mathbb{R}^{N \times r}$ and $V_r \in \mathbb{R}^{d \times r}$ have orthonormal columns. The orthogonal projector onto the row space of F_c is $\Pi_F = V_r V_r^\top$, and the row-space coherence is defined as $\mu \triangleq \frac{N}{r} \max_{i \in [N]} \|e_i^\top U_r\|_2^2 \in [1, N/r]$. Let $\mathcal{I} \subset [N]$ be a uniformly random subset of m indices without replacement, and let $F_{\mathcal{I}} \in \mathbb{R}^{m \times d}$ be the corresponding submatrix of F_c . Let $\Pi_{F_{\mathcal{I}}}$ denote the orthogonal projector onto the row space of $F_{\mathcal{I}}$. Then there exists a constant $C > 0$ such that, for any $\varepsilon, \delta \in (0, 1)$, if*

$$m \geq C \frac{\mu r}{\varepsilon^2} \log\left(\frac{r}{\delta}\right), \quad (6)$$

the following holds with probability at least $1 - \delta$:

$$\|\Pi_F - \Pi_{F_{\mathcal{I}}}\|_2 \leq \varepsilon, \quad (7)$$

i.e., the principal r -dimensional subspace of F_c is preserved. For the full proof, see section A.4.

4. Experimental results

We begin by empirically confirming that patch-wise features are redundant and highly correlated.

4.1. Redundancy analysis: qualitative and quantitative evidence

PCA explained variance over feature dimensions. Let $F \in \mathbb{R}^{N \times d}$ be the descriptor matrix. We visualize the cumulative explained variance $E(m)$ (as in (3)) as a function of the number of components used m . Fig. 3(a) shows that 90% of the variance is captured by 17 of 64 principal components. Repeating the analysis over the 128 patches with the highest norm, yields 90% with 14 components, which confirms that redundancy persists even among the strongest tokens. The experiment was conducted on 10000 frames from different scenes, and averaged across all.

Patch-wise correlation structure. We compute the Pearson correlation between all patch descriptors within a frame to obtain an $N \times N$ correlation matrix. A representative heatmap appears in Fig. 3(b), which shows extensive off-diagonal positive and negative correlation, indicating pervasive redundancy across spatial tokens.

Similarity overlays on the image plane example. For a seed patch i with descriptor $f_i \in \mathbb{R}^d$, we compute cosine similarities $s_j = \frac{f_i \cdot f_j}{\|f_i\| \|f_j\|}$ for all patches j , reshape $s \in \mathbb{R}^N$ to the $H' \times W'$ grid, upsample to the input resolution, and overlay it on the raw image with a heatmap. High intensity indicates semantic overlap. Examples for two seed locations are shown in Fig. 3(c). Widespread high similarity far from the seed in multiple locations illustrates global entanglement and redundancy. See Appx. A.2 for the full 16×16 grid of overlays for all patches.

These qualitative and quantitative results support our hypothesis that patch descriptors live in a low-dimensional subspace and exhibit strong cross-patch redundancy, explaining why stochastic sub-sampling maintains scene semantics.

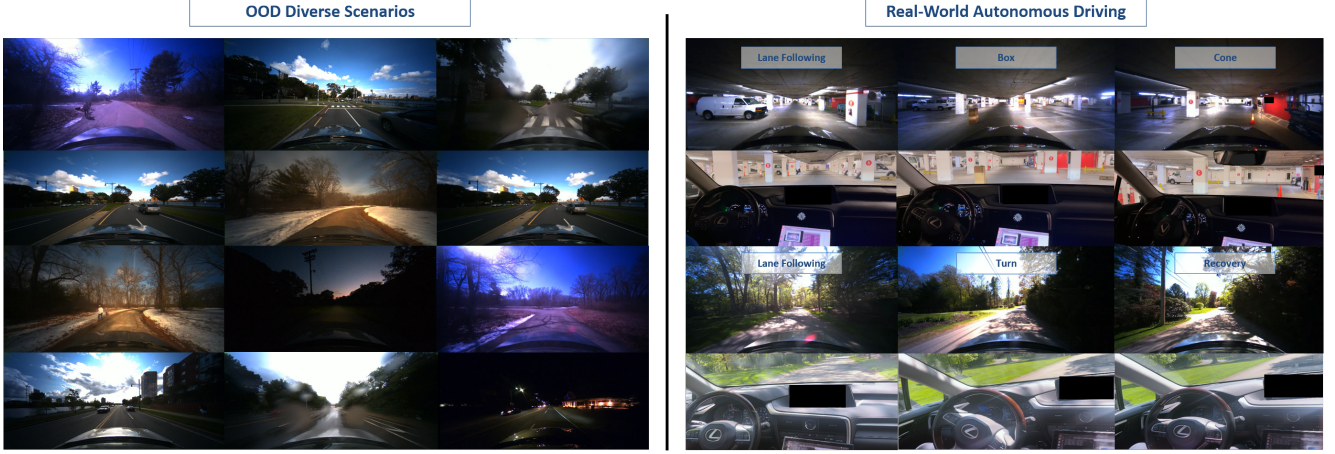


Figure 4. Left: Diverse OOD sample frames across varying seasons, weather, and lighting conditions. Right: Real-car deployment representative frames from the rural road (public park) and parking garage, captured from both the onboard camera and external view.

4.2. SPS Experimental settings

We conduct extensive closed-loop driving experiments both for in-distribution and OOD environments. Below, we detail the hardware, tasks, evaluation metrics, and training data.

Task definition and evaluation protocol. As in [3], we target a general-purpose autonomous driving task requiring the vehicle to follow lanes and avoid obstacles. Failure is defined by three conditions: (i) crossing lane boundaries, (ii) collisions or dangerously close proximity to objects, and (iii) heading deviations exceeding 30° from the lane direction. In simulation, we assess performance using a normalized success duration metric, measuring how long the vehicle drives without triggering any failure, averaged over 100 episodes of roughly 20 seconds each. In real-world testing, performance is quantified by counting safety driver interventions, following the same failure definitions. Evaluations are performed in a closed-loop manner unless otherwise specified.

Training data and learning framework. Our training data combines real-world driving logs with diverse simulated experiences generated using VISTA [12], a simulator built upon approximately two hours of real driving data captured across varied environments, lighting, and weather conditions. The learning procedure adopts Guided Policy Learning [12, 53], leveraging privileged simulator signals to supervise image-based control policies. Control labels are derived using a PID controller for lane keeping and Control Barrier Functions (CBFs) [9] for safety-aware obstacle avoidance. Policies are trained using the Adam optimizer (learning rate 10^{-3}), an L2 loss objective, and a plateau scheduler with patience 10 and no decay. We utilize BLIP-2 [4] as the feature extractor to enable a fair comparison with SOTA [3].

Vehicle platform and Hardware.

The real car experiments were conducted using a fully autonomous 2019 Lexus RX 450H equipped with high-performance computing and sensing hardware. The onboard system includes an NVIDIA RTX 4070 Ti GPU and an AMD Ryzen 7 3800X 8-core CPU. Visual input is captured via a BFS-PGE-23S3C-CS camera running at 30 frames per second, with a 130° horizontal field of view and a resolution of 960×600 pixels. The models were trained and evaluated on a university-managed cloud cluster using a total of four A100 GPUs (40GB each). Training took approximately four days.

4.3. OOD generalization

To contextualize our improvements, we adapt the OOD generalization experiments and benchmarks reported in the *Drive-Anywhere* [3] framework. Specifically, we train the model in rural environments during summer, under dry weather conditions and daytime lighting, with the presence of other vehicles on the road. We then evaluate its performance across diverse scenes, weather conditions, times of day, and in the presence of other dynamic actors.

Baselines: (i) No Foundation Model (*No-FM*) [8], [12], a baseline that trains a convolutional model without using foundation models (transformer-based variants performed similarly); (ii) *Mask-based Features (MF)* [29, 47], which segment the input image by applying a universal segmentation model [46], extracts a global feature vector for each region by applying a pretrained encoder [49] on a crop bounding this region, and assign that vector uniformly to all pixels within the mask. (iii) *Inherent ViT Features (I-ViT)* [52], which extract per-patch features from the output of intermediate layers of a ViT model [6], using the key, query, and value matrices as token-aligned visual descriptors, (iv)

Table 1. Benchmarking OOD generalization. [†]Indicates car types different from training. ID = in-distribution. OOD = out-of-distribution.

Setting	Scenarios					Methods				
	Scene	Season	Weather	Time	Actor	No-FM	Uni-modal FMF	Multi-modal FMF		
ID	Rural	Summer	Dry	Day	Car	1.00	1.00	MF	DA	SPS (Ours)
OOD	Rural	Spring	Dry	Day	Car [†]	0.84	0.86	0.42	0.96	0.98
		Summer	Dry	Night	Car [†]	0.30	0.80	0.35	0.89	0.92
		Fall	Dry	Day	Car [†]	0.90	0.95	0.74	0.91	0.96
		Winter	Snow	Day	Car [†]	0.14	0.88	0.42	0.96	0.99
		Spring	Dry	Day	Animal	0.85	0.89	0.39	0.95	0.99
		Summer	Dry	Night	Animal	0.29	0.59	0.39	0.85	0.86
		Fall	Dry	Day	Animal	0.87	0.95	0.71	0.88	0.93
	Urban	Winter	Snow	Day	Animal	0.15	0.87	0.45	0.95	0.99
		Summer	Dry	Day	Car [†]	0.55	0.77	0.50	0.62	0.82
		Summer	Rain	Day	Car [†]	0.69	0.81	0.43	0.81	0.83
	Average	Summer	Dry	Night	Car [†]	0.45	0.81	0.42	0.78	0.87
		Summer	Dry	Day	Animal	0.58	0.80	0.50	0.64	0.79
		Summer	Rain	Day	Animal	0.66	0.83	0.43	0.78	0.84
		Summer	Dry	Night	Animal	0.45	0.86	0.36	0.81	0.88
		Average				0.55	0.83	0.47	0.84	0.90
		Our increase (%) vs. other methods				↑ 35%	↑ 7%	↑ 53%	↑ 6%	-

the current SOTA Drive Anywhere (DA) [3], which creates per-patch descriptor via the masking strategy explained in Section 3.1, and ours; *SPS* as defined in Section 3.3 without adding any variant from 3.4, with a RATE = 0.5.

Discussion. The results are reported in Table 1. First, *MF* underperforms across both in-distribution and OOD settings, likely due to the applied masking model, which may miss and not segment part of the image [54], and thus exclude relevant information from the feature tensor. In contrast, *I-ViT* and *DA* outperform *No-FM*, underscoring the benefit of pretrained representations. However, *I-ViT* remains a uni-modal approach and does not incorporate language grounding. Finally, our proposed method, *SPS*, clearly outperforms all baselines, improving upon the previous SOTA (*DA*) by an average of 6% and up to 20% in specific OOD scenarios. Our improvement over each method is reported in the last row of the table. We provide examples in Fig. 4 for representative frames from diverse OOD conditions.

Other variants. We evaluate additional variants of *SPS* yielding nine different models in total, incorporating different architectural modifications (e.g., different RATE, position-adjusted, threshold masking). Figure 5 shows that 8 out of the 9 models outperform the strongest baseline in OOD settings, and Table 2 shows detailed results of all variants across each OOD scenario, demonstrating the robustness and flexibility of our approach; see Section 4.5 for details.

Cross-backbone generalization (DINO). We also applied *SPS* to a DINO backbone to test transfer beyond BLIP2. For brevity, we report in the appendix OOD scenarios that vary a lot from the in-distribution training set and are therefore especially challenging. On this subset, *SPS* improves DINO in 6 of 7 scenarios and ties in one, with an average absolute gain of +3.3%; see Table 5 in the Appendix.

4.4. Latent space text-augmented fine-tuning

We adapt language-guided latent space augmentation to further improve the robustness of our best model, *SPS-50%*. The augmentation pipeline proceeds as follows: (i) We prompt an LLM to produce a concise list of driving-relevant textual features; visual concepts present in the training scenes, e.g., *Tree* or *Truck*; these are then identified, and will plausibly be replaced to foster OOD generalization. (ii) An LLM is queried to generate alternative concepts that are visually plausible and commonly encountered in driving scenarios (e.g., *house* instead of *tree*). (iii) In selected frames, patch-level descriptors associated with the target concepts are replaced in latent space with those derived from the suggested alternatives using the foundation model’s text encoder. This results in a form of data augmentation that preserves scene coherence while introducing semantic diversity.

We apply this technique as a lightweight fine-tuning step to the pretrained *SPS-50%* model. The model is updated for a small number of iterations using augmented latent features. As shown in Table 3, this results in a further +1.7% accuracy

Table 2. *Ablating all of our variants for OOD generalization.* \dagger indicates car types different from training. *ID* is in distribution. *OOD* is out-of-distribution.

Setting	Scenarios					Methods										
	Scene	Season	Weather	Time	Actor	DA	MSPPS-70%	MSPPS-50%	MSPPS-30%	SPPS-70%	SPPS-50%	SPPS-30%	SPS-70%	SPS-50%	SPS-30%	
ID	Rural	Summer	Dry	Day	Car	1.00	1.00	1.00	1.00	1.00	1.00	1.00	1.00	1.00	1.00	
OOD	Rural	Spring	Dry	Day	Car \dagger	0.96	0.96	0.97	0.98	0.98	0.99	0.99	0.98	0.94		
		Summer	Dry	Night	Car \dagger	0.89	0.82	0.89	0.87	0.87	0.91	0.84	0.93	0.92	0.91	
		Fall	Dry	Day	Car \dagger	0.91	0.98	0.94	0.97	0.95	0.97	0.97	0.96	0.96	0.98	
		Winter	Snow	Day	Car \dagger	0.96	0.95	0.98	0.99	0.99	0.96	0.99	0.96	0.99	0.98	
		Spring	Dry	Day	Animal	0.95	0.95	0.97	0.97	0.97	0.98	0.95	0.95	0.99	0.95	
		Summer	Dry	Night	Animal	0.85	0.79	0.84	0.77	0.86	0.84	0.80	0.87	0.86	0.87	
	Urban	Fall	Dry	Day	Animal	0.88	0.99	0.91	0.94	0.93	0.97	0.92	0.97	0.93	0.92	
		Winter	Snow	Day	Animal	0.95	0.94	0.97	0.99	0.99	0.97	0.95	0.97	0.99	0.97	
		Summer	Dry	Day	Car \dagger	0.62	0.53	0.70	0.75	0.79	0.65	0.77	0.71	0.82	0.72	
		Summer	Rain	Day	Car \dagger	0.81	0.65	0.85	0.91	0.83	0.84	0.82	0.82	0.83	0.86	
		Summer	Dry	Night	Car \dagger	0.78	0.71	0.89	0.90	0.88	0.84	0.86	0.79	0.87	0.85	
		Summer	Dry	Day	Animal	0.64	0.50	0.65	0.72	0.76	0.64	0.74	0.73	0.79	0.70	
		Summer	Rain	Day	Animal	0.78	0.65	0.86	0.91	0.87	0.86	0.79	0.86	0.84	0.87	
		Summer	Dry	Night	Animal	0.81	0.71	0.88	0.90	0.89	0.85	0.86	0.85	0.88	0.90	
Average						84.2%	79.5%	88%	89.7%	89.7%	87.6%	87.5%	88.3%	90.4%	88.7%	
Our increase (%) vs. other methods						-	$\downarrow 4.7\%$	$\uparrow 3.8\%$	$\uparrow 5.5\%$	$\uparrow 5.5\%$	$\uparrow 3.4\%$	$\uparrow 3.3\%$	$\uparrow 4.1\%$	$\uparrow 6.2\%$	$\uparrow 4.5\%$	

Table 3. *Language-guided augmentation for OOD generalization.*

We fine-tune the pretrained SPS-50% model using language-driven latent feature substitution based on LLM-suggested concepts.

RSDDC	RSDNC	RFDDC	RWSDC	RSDDA
-	+0.29%	+1.85%	-	-
RSDNA	RFDDA	RWSDA	USDDC	USRDC
-0.21%	+2.93	-	-1.16	+4.39%
USDNC	USDDA	USRDA	USDNA	All
+0.36%	+3.86%	+3.28%	+1.43%	+1.7%

gain across OOD scenarios, excluding cases where the base model already achieves near-perfect performance ($\geq 98\%$), where meaningful further gains are unlikely. These results show that *SPS* effectively integrates semantic augmentations through an interpretable, text-driven process, enabling scalable generalization via concept-level latent edits.

4.5. Ablations: efficiency and performance

Beyond improving generalization, *SPS* offers substantial computational benefits during both training and inference. By selecting only a subset of patch features, we reduce the overall processing load without sacrificing semantic richness. We explore multiple variants leveraging the *SPS* mechanism.

Variants. In the base *SPS* variant, unselected patch descriptors are replaced with zeros, preserving the feature tensor’s original shape. In the more aggressive *SPPS* (*Structured Patch Pruning with Selection*), unselected tokens are entirely removed; the selected tokens are then spatially reorganized and assigned position embeddings relative to their original location (Method V2 from Section 3.4). A third variant, *MSPPS* (*Matrix-based Structured Patch Pruning*), stochastically prunes patch tokens based on a per-patch probability mask, yielding dynamic, matrix-based sparsity. Notably, it also prunes unselected patches as in *SPPS* (the combination

of V1 and V2 from section 3.4).

Speed reported results. Each variant is evaluated across three selection rates: 70%, 50%, and 30%. Inference timing was measured over 100 independent runs per model component, with averages reported for the QFormer, vision projection and normalization, BLIP2 convolution, and the ViT policy model. While we train and benchmark nine model variants in total, only six representative models are shown in Table 4, as the *SPPS* and *MSPPS* variants are functionally similar in terms of runtime, with any differences being negligible in practice. The *SPS-50%* model (our best model in terms of accuracy) achieves a $2.43\times$ speedup over the SOTA *Drive-Anywhere*. At the more aggressive 30% selection rate, *SPPS* and *SPS* reach $3.31\times$ and $3.47\times$ speedups, respectively. This shows the core trends: a consistent correlation between lower selection rates and improved runtime, highlighting that *SPS* not only improves generalization, but also enables substantial computational gains, making it attractive for real-world autonomous systems deployment.

Speed vs accuracy reported results. To analyse the trade-off between efficiency and accuracy, in Figure 1(4) we show a comparison, where each model is represented by a single node: The x-axis reflects runtime cost, defined as the inverse of the model’s speedup over the baseline $-1/T_{\text{Factor}}$ (lower is better), while the y-axis reports average closed-loop performance. Node color encodes a composite performance score, computed as accuracy divided by runtime (higher is better), highlighting models that strike the best balance between precision and efficiency. The six reported models gain better accuracy while being faster than the drive anywhere model; the improvements of our variant in terms of accuracy vary from 3.3% to 6.2%, while the speed improved $1.69\times$ to $3.47\times$. While our composite

Table 4. **Runtime Efficiency of SPS.** The calculations were averaged across 100 independent runs.

Model	Qformer		Vision Proj.&Norm		FM Project		Policy		Total Efficiency	
	Qformer	Efficiency	VP&N	Efficiency	FMC	Efficiency	Policy	Efficiency	Percentage	Factor
Benchmark	2.17s	–	871 μ s	–	540 μ s	–	17ms	–	100%	x1
SPS_70%	1.56s	39.10%	839 μ s	3.75%	376 μ s	43.67%	20ms	0.24%	86.52%	x1.87
SPS_50%	1.11s	95.50%	855 μ s	1.88%	370 μ s	46.08%	20ms	–1.22%	143.45%	x2.43
SPS_30%	0.71s	205.63%	842 μ s	3.45%	390 μ s	38.41%	20ms	0.41%	247.50%	x3.47
SPPS_70%	1.56s	39.10%	846 μ s	2.93%	500 μ s	8.06%	14.3ms	18.92%	69.02%	x1.69
SPPS_50%	1.11s	95.50%	837 μ s	4.06%	493 μ s	9.41%	14.5ms	17.45%	126.41%	x2.26
SPPS_30%	0.71s	205.63%	841 μ s	3.58%	542 μ s	–0.44%	13.9ms	22.43%	231.21%	x3.31

performance analysis (Fig. 1(4)) shows that *SPS-70%* and *SPPS-70%* achieve the highest scores when accuracy and runtime are equally weighted, practical deployment considerations suggest a different weighting scheme. In the context of real-world autonomous driving, reliability and generalization, particularly under OOD conditions, are of higher criticality than marginal gains in computational speed. The *SPS-50%* model consistently delivers the highest average accuracy across scenarios, and this performance margin is non-trivial in safety-critical systems. We therefore view *SPS-50%* as the strongest overall candidate for real-world deployment, offering the best tradeoff between robustness and efficiency.

The effect of RATE. As shown in Table 2, most variants outperform the *Drive-Anywhere* benchmark across OOD scenarios, with *SPS-50%* achieving the highest accuracy (+6.2%), highlighting the general effectiveness of stochastic patch selection. Figure 5 plots performance against selection rate for each variant, revealing distinct trends: *SPS* peaks at 50%, offering the strongest gain; *SPPS* performs best at 70% and declines with more aggressive pruning; and *MSPPS* improves as selection becomes stricter, peaking at 30%. These findings confirm that stochastic selection improves generalization across architectures, though the optimal ratio varies. Notably, moderate selection rates strike the best tradeoff between redundancy reduction and information retention in models where spatial structure is retained.

4.6. Real-world car deployment

We deployed the *SPS-50%* model on a full-scale autonomous vehicle (see supplementary video). The experiments took place during the spring season at two distinct locations: a rural road within a public park and an underground parking garage. In the rural scenario, the vehicle successfully performed lane-following under natural daylight conditions, confirming the model’s ability to transfer from simulation to the real world. The underground scenario was a challenging OOD test case, featuring low-light conditions, the absence of clear lanes, and visually cluttered geometry, such as perpen-

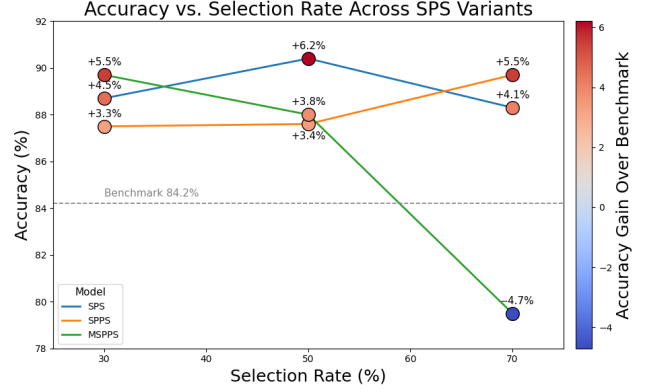


Figure 5. Accuracy as a function of selection rate across variants.

dicular parking lines, parked vehicles, and distractor objects. Despite never encountering such a configuration at training, the vehicle executed the correct motion. In addition, it successfully avoided static obstacles, including cones and boxes, further demonstrating its robustness. Representative frames from both real-world scenarios, captured from onboard and external views, are shown in Figure 4.

5. Conclusion and future work

This work shows that patch-aligned features (extracted from vision–language models) used for training driving policies are correlated and redundant. Motivated by this, it introduced SPS: a stochastic patch–masking strategy that tackles the redundancy inevitably built into such features. By randomly suppressing a fraction of patch descriptors while preserving their spatial arrangement, SPS forces the policy to ground its decisions on features that are robust to which tokens survive. Across a diverse suite of closed-loop driving scenarios, covering weather, lighting and geographic domain shifts, SPS delivers a **6.2%** average gain in OOD success rate, peaks at **20.4%** improvement in the hardest scenarios, and speeds inference by **2.4 \times** compared with the previous SOTA. The same mechanism enables text-conditioned data augmentation in the latent patch space, yielding more **1.7%** boost

without extra image synthesis. Ablations confirm that the benefit is robust to (reasonable) selection rates, selection methods, and feature re-ordering schemes: 8 out of the 9 trained systems surpassed the prior SOTA. We demonstrated that policies trained with SPS in simulation transfer to a real-world autonomous vehicle with *no* extra fine-tuning, highlighting the practical relevance of the approach.

Future work includes sophisticated selection techniques (i) learning a state-dependent sampling policy that select the number of patches to allocate based on scenes, and (ii) going beyond uniform sampling by *inspecting* the descriptors themselves, e.g., coresets selection, attention entropy, or mutual-information scores, to drop provably redundant patches, further sharpening both efficiency and robustness.

Acknowledgments

Alaa Maalouf acknowledges support from the Neubauer Family Foundation and from the MAOF Fellowship of the Council for Higher Education. This work is supported by Toyota Research Institute (TRI) and Capgemini Engineering. It, however, reflects solely the opinions and conclusions of its authors and not TRI or any other Toyota entity.

References

- [1] D. A. Pomerleau, “Alvinn: An autonomous land vehicle in a neural network,” *Advances in neural information processing systems*, vol. 1, 1988. [1](#), [2](#), [3](#)
- [2] M. Bojarski, D. Del Testa, D. Dworakowski, B. Firner, B. Flepp, P. Goyal, L. D. Jackel, M. Monfort, U. Muller, J. Zhang *et al.*, “End to end learning for self-driving cars,” *arXiv preprint arXiv:1604.07316*, 2016. [1](#), [2](#), [3](#)
- [3] T.-H. Wang, A. Maalouf, W. Xiao, Y. Ban, A. Amini, G. Rosman, S. Karaman, and D. Rus, “Drive anywhere: Generalizable end-to-end autonomous driving with multi-modal foundation models,” in *2024 IEEE International Conference on Robotics and Automation (ICRA)*, 2024, pp. 6687–6694. [2](#), [3](#), [6](#), [7](#)
- [4] J. Li, D. Li, S. Savarese, and S. Hoi, “Blip-2: Bootstrapping language-image pre-training with frozen image encoders and large language models,” *arXiv preprint arXiv:2301.12597*, 2023. [2](#), [3](#), [6](#)
- [5] J. Li, D. Li, C. Xiong, and S. Hoi, “Blip: Bootstrapping language-image pre-training for unified vision-language understanding and generation,” in *International Conference on Machine Learning*. PMLR, 2022, pp. 12 888–12 900. [3](#)
- [6] H. Zhang, F. Li, S. Liu, L. Zhang, H. Su, J. Zhu, L. M. Ni, and H.-Y. Shum, “Dino: Detr with improved denoising anchor boxes for end-to-end object detection,” 2022. [2](#), [6](#)
- [7] A. Amini, G. Rosman, S. Karaman, and D. Rus, “Variational end-to-end navigation and localization,” in *2019 International Conference on Robotics and Automation (ICRA)*. IEEE, 2019, pp. 8958–8964. [2](#), [3](#)
- [8] T.-H. Wang, W. Xiao, M. Chahine, A. Amini, R. Hasani, and D. Rus, “Learning stability attention in vision-based end-to-end driving policies,” in *Learning for Dynamics and Control Conference*. PMLR, 2023, pp. 1099–1111. [2](#), [6](#)
- [9] W. Xiao and C. Belta, “Control barrier functions for systems with high relative degree,” in *Proc. of 58th IEEE Conference on Decision and Control*, Nice, France, 2019, pp. 474–479. [2](#), [6](#)
- [10] W. Xiao, T.-H. Wang, R. Hasani, M. Chahine, A. Amini, X. Li, and D. Rus, “Barriernet: Differentiable control barrier functions for learning of safe robot control,” *IEEE Transactions on Robotics*, 2023. [2](#), [3](#)
- [11] A. Kendall, J. Hawke, D. Janz, P. Mazur, D. Reda, J.-M. Allen, V.-D. Lam, A. Bewley, and A. Shah, “Learning to drive in a day,” in *2019 International Conference on Robotics and Automation (ICRA)*. IEEE, 2019, pp. 8248–8254. [2](#)
- [12] A. Amini, T.-H. Wang, I. Gilitschenski, W. Schwarting, Z. Liu, S. Han, S. Karaman, and D. Rus, “Vista 2.0: An open, data-driven simulator for multimodal sensing and policy learning for autonomous vehicles,” in *2022 International Conference on Robotics and Automation (ICRA)*. IEEE, 2022, pp. 2419–2426. [2](#), [6](#)
- [13] A. Dosovitskiy, G. Ros, F. Codevilla, A. Lopez, and V. Koltun, “Carla: An open urban driving simulator,” in *Conference on robot learning*. PMLR, 2017, pp. 1–16. [2](#)
- [14] S. Shah, D. Dey, C. Lovett, and A. Kapoor, “Airsim: High-fidelity visual and physical simulation for autonomous vehicles,” in *Field and Service Robotics: Results of the 11th International Conference*. Springer, 2018, pp. 621–635.
- [15] R. Tedrake *et al.*, “Drake: Model-based design and verification for robotics,” 2019, software Package, available at <https://drake.mit.edu/>. [2](#)
- [16] M. Müller, A. Dosovitskiy, B. Ghanem, and V. Koltun, “Driving policy transfer via modularity and abstraction,” *arXiv preprint arXiv:1804.09364*, 2018. [2](#)
- [17] M. Toromanoff, E. Wirbel, and F. Moutarde, “End-to-end model-free reinforcement learning for urban driving using implicit affordances,” in *Proceedings of the IEEE/CVF conference on computer vision and pattern recognition*, 2020, pp. 7153–7162.
- [18] A. Behl, K. Chitta, A. Prakash, E. Ohn-Bar, and A. Geiger, “Label efficient visual abstractions for autonomous driving,” in *2020 IEEE/RSJ International Conference on Intelligent Robots and Systems (IROS)*. IEEE, 2020, pp. 2338–2345. [2](#)
- [19] S. Tellex, N. Gopalan, H. Kress-Gazit, and C. Matuszek, “Robots that use language,” *Annual Review of Control, Robotics, and Autonomous Systems*, vol. 3, pp. 25–55, 2020. [2](#)
- [20] Y. Bisk, A. Holtzman, J. Thomason, J. Andreas, Y. Bengio, J. Chai, M. Lapata, A. Lazaridou, J. May, A. Nisnevich *et al.*, “Experience grounds language,” *arXiv preprint arXiv:2004.10151*, 2020.
- [21] M. Ahn, A. Brohan, N. Brown, Y. Chebotar, O. Cortes, B. David, C. Finn, C. Fu, K. Gopalakrishnan, K. Hausman *et al.*, “Do as i can, not as i say: Grounding language in robotic affordances,” *arXiv preprint arXiv:2204.01691*, 2022.
- [22] A. Brohan, N. Brown, J. Carbalal, Y. Chebotar, J. Dabis, C. Finn, K. Gopalakrishnan, K. Hausman, A. Herzog, J. Hsu *et al.*, “Rt-1: Robotics transformer for real-world control at scale,” *arXiv preprint arXiv:2212.06817*, 2022.

- [23] S. Li, X. Puig, C. Paxton, Y. Du, C. Wang, L. Fan, T. Chen, D.-A. Huang, E. Akyürek, A. Anandkumar *et al.*, “Pre-trained language models for interactive decision-making,” *Advances in Neural Information Processing Systems*, vol. 35, pp. 31 199–31 212, 2022. [2](#)
- [24] M. Barbara and A. Maalouf, “Prompts to summaries: Zero-shot language-guided video summarization,” *arXiv preprint arXiv:2506.10807*, 2025. [2](#)
- [25] C. Huang, O. Mees, A. Zeng, and W. Burgard, “Audio visual language maps for robot navigation,” *arXiv preprint arXiv:2303.07522*, 2023. [2](#)
- [26] R. Ding, J. Yang, C. Xue, W. Zhang, S. Bai, and X. Qi, “Pla: Language-driven open-vocabulary 3d scene understanding,” in *Proceedings of the IEEE/CVF Conference on Computer Vision and Pattern Recognition*, 2023, pp. 7010–7019.
- [27] S. Peng, K. Genova, C. Jiang, A. Tagliasacchi, M. Pollefeys, T. Funkhouser *et al.*, “Openscene: 3d scene understanding with open vocabularies,” in *Proceedings of the IEEE/CVF Conference on Computer Vision and Pattern Recognition*, 2023, pp. 815–824. [2](#)
- [28] M. Chahine, A. Quach, A. Maalouf, T.-H. Wang, and D. Rus, “Flex: End-to-end text-instructed visual navigation with foundation models,” 2024. [Online]. Available: <https://arxiv.org/abs/2410.13002> [2](#), [3](#)
- [29] A. Maalouf, N. Jadhav, K. M. Jatavallabhula, M. Chahine, D. M. Vogt, R. J. Wood, A. Torralba, and D. Rus, “Follow anything: Open-set detection, tracking, and following in real-time,” *arXiv preprint arXiv:2308.05737*, 2023. [2](#), [6](#)
- [30] S. Liu, Z. Zeng, T. Ren, F. Li, H. Zhang, J. Yang, C. Li, J. Yang, H. Su, J. Zhu *et al.*, “Grounding dino: Marrying dino with grounded pre-training for open-set object detection,” *arXiv preprint arXiv:2303.05499*, 2023.
- [31] G. Ghiasi, X. Gu, Y. Cui, and T.-Y. Lin, “Scaling open-vocabulary image segmentation with image-level labels,” in *Computer Vision–ECCV 2022: 17th European Conference, Tel Aviv, Israel, October 23–27, 2022, Proceedings, Part XXXVI*. Springer, 2022, pp. 540–557.
- [32] B. Li, K. Q. Weinberger, S. Belongie, V. Koltun, and R. Ranftl, “Language-driven semantic segmentation,” *arXiv preprint arXiv:2201.03546*, 2022.
- [33] M. Chahine, W. Yang, A. Maalouf, J. Siriska, N. Jadhav, D. Vogt, S. Gil, R. Wood, and D. Rus, “Decentralized vision-based autonomous aerial wildlife monitoring,” *arXiv preprint arXiv:2508.15038*, 2025. [2](#)
- [34] A. Ramesh, M. Pavlov, G. Goh, S. Gray, C. Voss, A. Radford, M. Chen, and I. Sutskever, “Zero-shot text-to-image generation,” in *International Conference on Machine Learning*. PMLR, 2021, pp. 8821–8831. [2](#)
- [35] K. Crowson, S. Biderman, D. Kornis, D. Stander, E. Hallahan, L. Castricato, and E. Raff, “Vqgan-clip: Open domain image generation and editing with natural language guidance,” in *European Conference on Computer Vision*. Springer, 2022, pp. 88–105.
- [36] O. Patashnik, Z. Wu, E. Shechtman, D. Cohen-Or, and D. Lischinski, “Styleclip: Text-driven manipulation of stylegan imagery,” in *Proceedings of the IEEE/CVF International Conference on Computer Vision*, 2021, pp. 2085–2094.
- [37] A. Ramesh, P. Dhariwal, A. Nichol, C. Chu, and M. Chen, “Hierarchical text-conditional image generation with clip latents,” *arXiv preprint arXiv:2204.06125*, 2022. [2](#)
- [38] S. Sreeram, T.-H. Wang, A. Maalouf, G. Rosman, S. Karaman, and D. Rus, “Probing multimodal llms as world models for driving,” *IEEE Robotics and Automation Letters*, vol. 10, no. 11, pp. 11403–11410, 2025. [2](#)
- [39] J. Kim, T. Misu, Y.-T. Chen, A. Tawari, and J. Canny, “Grounding human-to-vehicle advice for self-driving vehicles,” in *Proceedings of the IEEE/CVF Conference on Computer Vision and Pattern Recognition (CVPR)*, Nov. 2019, pp. 10 591–10 599. [3](#)
- [40] D. Omeiza, H. Webb, M. Jiroka, and L. Kunze, “Explanations in autonomous driving: A survey,” *IEEE Transactions on Intelligent Transportation Systems*, vol. 23, no. 8, pp. 10 142–10 162, 2021.
- [41] Y.-L. Kuo, X. Huang, A. Barbu, S. G. McGill, B. Katz, J. J. Leonard, and G. Rosman, “Trajectory prediction with linguistic representations,” in *2022 International Conference on Robotics and Automation (ICRA)*. IEEE, 2022, pp. 2868–2875.
- [42] S. Tan, B. Ivanovic, X. Weng, M. Pavone, and P. Krahenbuehl, “Language conditioned traffic generation,” *arXiv preprint arXiv:2307.07947*, 2023.
- [43] Z. Zhong, D. Rempe, Y. Chen, B. Ivanovic, Y. Cao, D. Xu, M. Pavone, and B. Ray, “Language-guided traffic simulation via scene-level diffusion,” *arXiv preprint arXiv:2306.06344*, 2023. [3](#)
- [44] M. Caron, H. Touvron, I. Misra, H. Jégou, J. Mairal, P. Bojanowski, and A. Joulin, “Emerging properties in self-supervised vision transformers,” in *Proceedings of the IEEE/CVF international conference on computer vision*, 2021, pp. 9650–9660. [3](#)
- [45] M. Oquab, T. Darcret, T. Moutakanni, H. Vo, M. Szafraniec, V. Khalidov, P. Fernandez, D. Haziza, F. Massa, A. El-Nouby *et al.*, “Dinov2: Learning robust visual features without supervision,” *arXiv preprint arXiv:2304.07193*, 2023. [3](#)
- [46] A. Kirillov, E. Mintun, N. Ravi, H. Mao, C. Rolland, L. Gustafson, T. Xiao, S. Whitehead, A. C. Berg, W.-Y. Lo *et al.*, “Segment anything,” *arXiv preprint arXiv:2304.02643*, 2023. [3](#), [6](#)
- [47] X. Zhao, W. Ding, Y. An, Y. Du, T. Yu, M. Li, M. Tang, and J. Wang, “Fast segment anything,” 2023. [6](#)
- [48] B. Cheng, I. Misra, A. G. Schwing, A. Kirillov, and R. Girdhar, “Masked-attention mask transformer for universal image segmentation,” in *Proceedings of the IEEE/CVF Conference on Computer Vision and Pattern Recognition*, 2022, pp. 1290–1299.
- [49] A. Radford, J. W. Kim, C. Hallacy, A. Ramesh, G. Goh, S. Agarwal, G. Sastry, A. Askell, P. Mishkin, J. Clark *et al.*, “Learning transferable visual models from natural language supervision,” in *International conference on machine learning*. PMLR, 2021, pp. 8748–8763. [6](#)
- [50] Y. Zhong, J. Yang, P. Zhang, C. Li, N. Codella, L. H. Li, L. Zhou, X. Dai, L. Yuan, Y. Li *et al.*, “Regionclip: Region-based language-image pretraining,” in *Proceedings of the IEEE/CVF Conference on Computer Vision and Pattern Recognition*, 2022, pp. 16 793–16 803.

- [51] K. M. Jatavallabhula, A. Kuwajerwala, Q. Gu, M. Osama, T. Chen, A. Maalouf, S. Li, G. Iyer, S. Saryazdi, N. Keetha *et al.*, “Conceptfusion: Open-set multimodal 3d mapping,” *arXiv preprint arXiv:2302.07241*, 2023. [3](#)
- [52] S. Amir, Y. Gandelsman, S. Bagon, and T. Dekel, “Deep ViT features as dense visual descriptors,” *arXiv preprint arXiv:2112.05814*, 2021. [3](#), [6](#)
- [53] S. Levine and V. Koltun, “Guided policy search,” in *International conference on machine learning*. PMLR, 2013, pp. 1–9. [6](#)
- [54] J. Dai, K. He, and J. Sun, “Convolutional feature masking for joint object and stuff segmentation,” in *2015 IEEE Conference on Computer Vision and Pattern Recognition (CVPR)*. IEEE, Jun. 2015. [7](#)

A. Appendix

A.1. PCA and correlation analysis: definitions and rationale

Feature covariance. Let F_c be an $N \times D$ matrix of the N computed patch descriptors. Assume F_c is centered (otherwise do so). Then compute $\Sigma = \frac{1}{N-1} F_c^\top F_c \in \mathbb{R}^{d \times d}$. The total variance equals the trace of Σ , which is the sum of eigenvalues. The cumulative explained variance curve reports $\sum_{i=1}^m \lambda_i / \sum_{i=1}^d \lambda_i$.

Top-energy subset. Let f_j denote the computed descriptor for patch j . Compute $\|f_i\|_2$ for each patch, sort, and keep the top 128 patches. Recompute the PCA curve on this subset. Achieving 90% variance with about 14 components indicates redundancy even among the strongest tokens.

Why feature-space PCA supports patch masking. Although SPS masks patches rather than feature channels, a low-rank feature manifold implies that many patches project into the same few directions. Removing some rows of F preserves the principal subspace with high probability, so semantics remain available from the retained tokens. One can also analyze patch-wise covariance $\frac{1}{d-1} F_c F_c^\top \in \mathbb{R}^{N \times N}$, which shows many correlated patches, consistent with the qualitative overlays in Appx. A.2.

Second-moment viewpoint. The matrix $F_c^\top F_c$ is the second-moment (Gram) matrix of descriptors. When we uniformly sample m rows without replacement to form SF_c , the expected Gram matrix of the sampled descriptors satisfies $\mathbb{E}[(SF_c)^\top (SF_c)] = \frac{m}{N} F_c^\top F_c$. Thus a quadratic form induced by the sampled rows preserves the full quadratic form in expectation up to the known scale m/N .

A.2. Full grid similarity overlays

How to compute it? Given $F_c \in \mathbb{R}^{N \times d}$ be the matrix of patch features as before, and let f_j denote the computed descriptor for patch j . Choose a seed index/patch i and define $s_j = \frac{f_i \cdot f_j}{\|f_i\| \|f_j\|}$ for every patch j . Set $s = (s_1, \dots, s_N)$, and reshape s to form $H' \times W'$ matrix, then upsample the matrix to the input resolution, and normalize to $[0, 1]$ and overlay with the original input frame F .

Interpretation of Fig. 6. Blue denotes low or negative cosine similarity and red denotes high positive similarity. For a given seed patch, only a sparse set of regions are strongly similar (red), while most are weakly or negatively related (blue). As the seed changes across the grid, the red regions shift to locations that share semantics with the new seed, illustrating globally entangled yet redundant representations.

A.3. DINO backbone results on Animal OOD scenarios

We also evaluate SPS with the DINO backbone (to show generalization across different setups/backbones) and observe consistent gains (Table 5).

Table 5. SPS with a DINO backbone on Animal OOD scenarios. These actors were not present in the in-distribution training set. SPS improves DINO in 6 of 7 scenarios and ties in one.

Scenario	DINO	DINO + SPS	Gain
RSpDDA	0.89	0.96	+7%
RSuDNA	0.59	0.65	+6%
RFDDA	0.95	0.97	+2%
RWSDA	0.87	0.92	+5%
USuDDA	0.80	0.82	+2%
USuRDA	0.83	0.83	0%
USuDNA	0.86	0.87	+1%
Average	82.7%	86%	+3.3%

A.4. Proof of Lemma 1

Proof of Lemma 1. **Step 0: Thin SVD, projectors, and coherence.** Let the thin SVD of the centered descriptor matrix be $F_c = U_r \Sigma_r V_r^\top$, with $U_r \in \mathbb{R}^{N \times r}$ and $V_r \in \mathbb{R}^{d \times r}$ having orthonormal columns, and $\Sigma_r \in \mathbb{R}^{r \times r}$ diagonal with positive entries. The projector onto the row space is $\Pi_F = V_r V_r^\top$. Define the uniform row coherence $\mu \triangleq \frac{N}{r} \max_{i \in [N]} \|(U_r)_{i:}\|_2^2 \in [1, N/r]$. Fix tolerances $\varepsilon \in (0, 1)$ and $\delta \in (0, 1)$.

Step 1: Second-moment identity in expectation. Let $S \in \{0, 1\}^{m \times N}$ select m rows uniformly without replacement, and write SF_c for the sampled submatrix. Then $S^\top S = \text{diag}(c_1, \dots, c_N)$ with $c_i \in \{0, 1\}$ indicating whether row i is selected, so $\mathbb{E}[S^\top S] = \frac{m}{N} I$ and

$$\mathbb{E}[(SF_c)^\top (SF_c)] = F_c^\top \mathbb{E}[S^\top S] F_c = \frac{m}{N} F_c^\top F_c. \quad (8)$$

Hence the second-moment (Gram) matrix of sampled descriptors preserves the full one in expectation up to the factor m/N .

Step 2: Subspace embedding via uniform row sampling. By matrix Chernoff concentration with bounded coherence (standard subspace-embedding results), if

$$m \geq C \frac{\mu r}{\varepsilon^2} \log\left(\frac{r}{\delta}\right),$$

then with probability at least $1 - \delta$ we have the spectral sandwich

$$(1 - \varepsilon) I_r \preceq \frac{N}{m} U_r^\top S^\top S U_r \preceq (1 + \varepsilon) I_r. \quad (9)$$

In particular, $U_r^\top S^\top S U_r$ is positive definite, so SU_r has full column rank r . By (9), all eigenvalues of $\frac{N}{m} U_r^\top S^\top S U_r$ lie in $[1 - \varepsilon, 1 + \varepsilon]$, hence $U_r^\top S^\top S U_r \succ 0$. Positive definiteness implies that for any $x \neq 0$, $x^\top U_r^\top S^\top S U_r x > 0$; therefore $SU_r x \neq 0$ and $\text{rank}(SU_r) = r$. This means the sampled rows still span an r -dimensional subspace in \mathbb{R}^N .

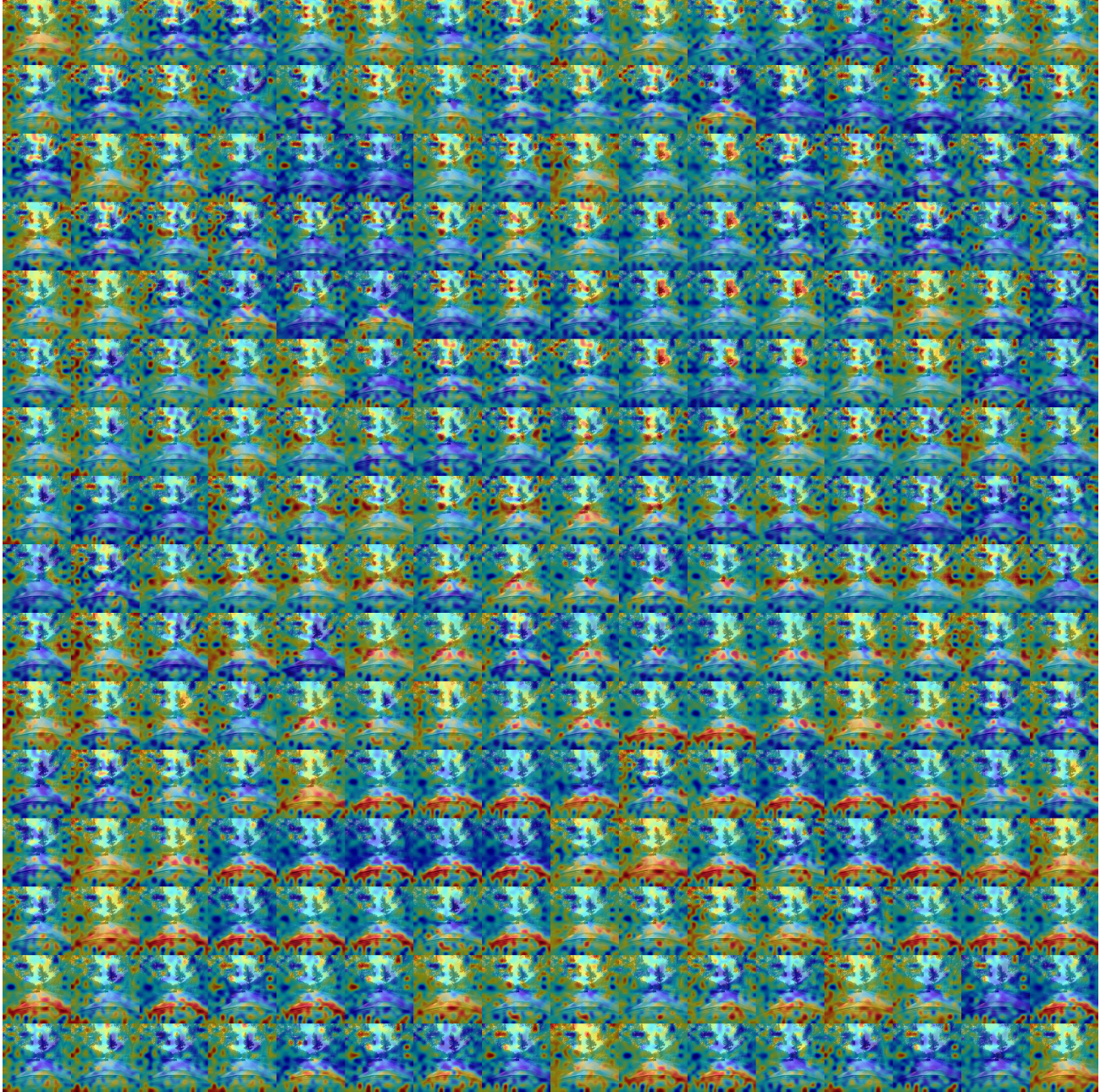


Figure 6. Full grid of similarity overlays for all 16×16 patches. Each cell shows the raw image overlaid with the cosine similarity from the corresponding seed patch to all other patches.

Step 3: Consequences for the row space. Using $F_c = U_r \Sigma_r V_r^\top$,

$$\begin{aligned} (SF_c)^\top (SF_c) &= V_r \Sigma_r (U_r^\top S^\top S U_r) \Sigma_r V_r^\top \\ &= V_r [\Sigma_r (U_r^\top S^\top S U_r) \Sigma_r] V_r^\top. \end{aligned} \quad (10)$$

Since $U_r^\top S^\top S U_r$ is $r \times r$ positive definite, the nonzero eigenvectors of $(SF_c)^\top (SF_c)$ are the columns of V_r , and the corresponding eigenvalues are those of $\Sigma_r (U_r^\top S^\top S U_r) \Sigma_r$.

Thus $(SF_c)^\top (SF_c)$ has the same nonzero eigenvectors as V_r , whose columns span $\text{span}(V_r)$. Consequently, the range of $(SF_c)^\top (SF_c)$ equals $\text{span}(V_r)$, so the row space of SF_c coincides with that of F_c , and the orthogonal projectors satisfy $\Pi_{SF_c} = \Pi_F$. This is stronger than the bound $\|\Pi_F - \Pi_{SF_c}\|_2 \leq \varepsilon$, which follows immediately.

Combining Steps 1–3 proves the lemma under the stated sample complexity. \square

Remark 1 (Lipschitz stability). Let ϕ be a row-wise Lipschitz map with constant L (for example, a per-token linear map followed by a 1-Lipschitz normalization). Let ϕ act independently on each row. Then

$$\begin{aligned}\|\phi(SF_c) - \phi(F_c)\|_F^2 &= \sum_{i=1}^N \|\phi((SF_c)_{i:}) - \phi((F_c)_{i:})\|_2^2 \\ &\leq \sum_{i=1}^N L^2 \|(SF_c)_{i:} - (F_c)_{i:}\|_2^2 \\ &= L^2 \|SF_c - F_c\|_F^2,\end{aligned}\tag{11}$$

so $\|\phi(SF_c) - \phi(F_c)\|_F \leq L \|SF_c - F_c\|_F$. Standard bounded-difference or matrix Bernstein arguments for sampling without replacement yield concentration of this deviation as m grows.

Remark 2 (Unbiased quadratic forms and covariance).

For any per-token linear map $\phi(X) = XW$,

$$\mathbb{E}[(SF_c)W^\top (SF_c)W] = \frac{m}{N} (F_cW)^\top (F_cW).\tag{12}$$

Thus quadratic objectives and covariances computed from the sampled rows preserve the full counterparts in expectation up to a known scale m/N . One can reweight by N/m , or rely on normalization layers to absorb the scale.

Covariance remark. Let $\widehat{\Sigma}_m \triangleq \frac{1}{m-1} (SF_c)^\top (SF_c)$ be the usual unbiased sample covariance built from the sampled rows, and $\widehat{\Sigma}_N \triangleq \frac{1}{N-1} F_c^\top F_c$ the full-sample covariance. Then

$$\begin{aligned}\mathbb{E}[\widehat{\Sigma}_m] &= \frac{1}{m-1} \mathbb{E}[(SF_c)^\top (SF_c)] = \frac{m}{N(m-1)} F_c^\top F_c \\ &= \frac{N-1}{N} \cdot \frac{m}{m-1} \widehat{\Sigma}_N.\end{aligned}\tag{13}$$

The factor $\alpha \triangleq \frac{N-1}{N} \cdot \frac{m}{m-1}$ is close to 1 whenever m and N are moderate to large. For $m = N/2$, $\alpha = \frac{N-1}{N} \cdot \frac{N}{N-2} = \frac{N-1}{N-2} = 1 + O(1/N)$. Hence the covariance is preserved in expectation up to a negligible finite-sample correction. In practice, either explicit reweighting (N/m) or standard normalization layers absorb any global scale, and the subspace preservation of Steps 2–3 is unaffected by scale.

A.5. Self Attensin Causes the Patch Redundancy

Self-attention mixing. Given a patch embedding matrix $X \in \mathbb{R}^{N \times D}$, a transformer layer forms $Q = XW^Q$, $K = XW^K$, and $V = XW^V$ with learned projections. The attention logits are $G = QK^\top$, and the token update is

$$Y = \text{SoftMax}(G)V \in \mathbb{R}^{N \times D}.\tag{14}$$

Hence, each output token Y_i is a convex combination of all value vectors V_j that are weighted by content similarity through the softmax of $Q_i K_j^\top$. This induces global mixing of information across tokens, so the descriptor at each spatial location carries scene-wide context.